Simulating damage onset and evolution in fully bio-resorbable composite under three-point bending

Xi Gao[1], Menghao Chen[2], Xiaogang Yang[1], Lee Harper[2], Ifty Ahmed[2], Jiawa Lu[1*]

[1] International Doctoral Innovation Centre, University of Nottingham Ningbo China, 315100, China

[2] Faculty of Engineering, University of Nottingham, NG7 2RD, United Kingdom

[*] Corresponding author: mailto: jiawa.lu@nottingham.edu.cn

Abstract

This paper presents a strain-based damage model to predict the stress-strain relationship and investigate the damage onset and evolution of the fibre and matrix of a fully bio-resorbable phosphate glass fibre reinforced composite under three-point bending. The flexural properties of the composite are crucial, particularly when it is employed as implant for long bone fracture. In the model, the 3D case of the strain and stress was used and the response of the undamaged material was assumed to be linearly elastic. The onset of damage was indicated by two damage variables for the fibre and matrix, respectively. The damage evolution law was based on the damage variable and the facture energy of the fibre and matrix, individually. A finite element (FE) model was created to implement the constitutive model and conduct numerical tests. An auto-adaptive algorithm is integrated in the FE model to improve the convergence. The FE model was capable of predicting the flexural modulus with around 3% relative error, and the flexural strength within 2% relative error in comparison with the experimental data. The numerical indices showed that the top surface of the sample was the most vulnerable under three-point bending. It was also found that the damage initiated in the fibre, was the primary driver for composite failure under three-point bending.

Key words: continuum damage mechanics, flexural strength, finite element analysis, bio-resorbable composite

1. Introduction

Traditionally, load-bearing metal implants have been used in surgical procedures for bone fixation purposes. However, these implants are commonly associated with the 'stress shielding' effect, which weakens the surrounding bone and increases the risk of re-fracture after the device has been removed [1-4]. Bio-resorbable implants provide an opportunity to match the properties of bone whilst transferring load to the healing bone more appropriately, along with being easily formed and their degradation products should be tolerated by the human body. There are reports of the application of fully bio-resorbable polymers as bone fracture fixation devices such as plates, screws, pins, and rods [4-6]. However, un-reinforced polymer implants have insufficient stiffness, particularly for load-bearing applications [7, 8]. The ideal replacement for traditional metallic bone fixation devices should have excellent biocompatibility, be fully bio-resorbable and have sufficient mechanical properties to support the bone during the early healing stages, before gradually degrading over time [4, 6, 9, 10]. A composite comprising polylactide (PLA) matrix reinforced with phosphate glass fibre (PGF) has been regarded as a

desirable reinforcement because of the mechanical properties it has achieved and it is fully bio-resorbable, releasing calcium and phosphate ions which are ideal for bone repair applications [11, 12]. Considerable effort has been put into investigating the mechanical properties of these materials [4, 9, 13-15], particularly the flexural strength [16-18], however damage initiation and accumulation in the fibre and matrix under three-point bending has not been investigated before. Therefore, the current paper seeks to develop an effective approach to assess the damage accumulation and resulting reduction in flexural performance of this bio-resorbable glass fibre reinforced polymer composite. Knowledges about the damage onset and evolution of the fibre and matrix extracted from this study are beneficial to the manufacturing of this type of composites, e.g. the selection of the fibre and matrix materials, the improving of manufacturing method, and possible optimization of fibre/matrix configuration. Subsequently, the results of this study are useful for pushing the research of employing bio-resorbable composites as bone fixation device material forward, which, ultimately, is beneficial to patients in the need of using bone fixation devices.

Damage initiation and evolution in the composite can be described using continuum damage mechanics (CDM), as long as the problem size is assumed to be sufficiently larger than the defect/microcrack size, to facilitate homogenisation [19]. Typically, a progressive damage model (PDM) consists of three steps: stress analysis, material properties degradation and failure analysis [20-22]. The crucial part of a PDM is to appropriately define the damage initiation criterion and evolution law. For unidirectional fibre reinforced composites, early work by Hill [23] was adopted by Tsai [24] to simulate the damage initiation in fibre reinforced composites. Hill's model was only intended for anisotropic ductile metals, and the yield stress in tension and compression were considered to be the same, which is unrealistic for the bio-resorbable composites whose compressive and tensile strength are different. Hoffman [25] later proposed a phenomenological fracture condition for orthotropic brittle materials which was capable of simulating the different properties of fibre reinforced composites in both the longitudinal and transverse directions. Hoffman developed Hill's model to consider different tensile and compressive yield stresses. However, both models lacked the capability of simulating the onset and evolution of damage. Matzenmiller *et al*. [26] proposed a damage model based on Hashin's criterion [27] involving five damage variables to simulate the elastic-brittle nature of the fibre reinforced composites. The tensile and compressive damage was modelled for both fibre and matrix, respectively. The 3D-Hashin and Tsai-Wu failure criteria were adopted to describe the damage initiation of yarns [28], in which the damage evolution of composites was strongly dependent on the reduction coefficients, which were controlled by the local stress and strain. Zhou *et al*. [29] and Fang *et al*. [30] proposed a modified 3D-Hashin failure criterion to model the damage initiation and evolution, and the reduction coefficients introduced by Murakami's theory [31] was adopted which were controlled by the equivalent stresses and equivalent strains. For these Hashin and Tasi-Wu based criterion, at least six different damage mechanisms were included, leading to a large number of equations which resulted in high computational cost. Linde *et al*. [32] developed a 2D criterion for progressive damage of fibre metal laminates, which was based on a strain-based continuum damage mechanics. Unlike Matzenmiller's model, Linde's model integrated the tensile and compressive damage as two damage variables for the fibre and matrix, respectively, but required the tensile and compressive strength of the fibre and matrix as input parameters. Lu *et al*. [33] extended the 2D failure criterion to 3D and adopted it to model the tensile properties of 3D braided composites. In both Linde's model and the modified model by Lu et al., the shear strain in the fibre direction was not part of the damage formulation. In the work of Chengyu et al. [34], a modified 3D model based on Linde's model was proposed to simulate the damage onset and failure for braided composites, in which the shear strain was taken into account and a better prediction was obtained (the relative error between the numerical and experimental results was reduced from 7.74% to 3.18% for the tensile strength and from 1.02% to 0.41% for the tensile modulus, see [33, 34]).

In this paper, the modified Linde's model in [34] has been adopted to simulate the three-point bending of a bio-resorbable composite. The model is three dimensional and takes into account shear strain in the fibre direction. The bio-resorbable composite modelled in this paper is a unidirectional continuous glass fibre reinforced polymer, which exhibits transversely isotropic properties. The constitutive model has been implemented in an FE environment, and an auto-adaptive algorithm has been integrated to improve convergence. The FE model is capable of capturing the onset and evolution of damage in the fibre and matrix under three-point bending. The numerical modelling in this paper is conducted by using the commercial FE software ABAQUS 6.13.

2. Experiment description

Three-point bending experiments were conducted on a Bose ElectroForce® Series II 3320 testing machine, following the British Standard (EN ISO 14125:1998+A1) to determine the flexural properties. The dimensions of the samples were manufactured as 40mm×15mm×2mm. During sample testing, the specimens were placed on two round supports with radius of 2mm at a span of 32mm. The load was applied vertically at the centre line of the specimen by a round cross-head loading member with a radius of 5mm. The temperature throughout the test was kept at room temperature (~22ºC) to exclude the thermal influence. Displacement/deflection loads were measured via the testing machine, for which the stress and strain were calculated according to the equations below:

$$\sigma_f = \frac{3FL}{2bh^2} \tag{1}$$

$$\varepsilon_f = \frac{6sh}{L^2} \tag{2}$$

where σ_f is the flexural stress, F is the applied load, ε_f is the flexural strain, s is the measured vertical displacement, L, b and h are the span, width, and thickness of the specimen, respectively.

3. Determination of the material constants

The continuous long fibre-reinforced composite exhibits transverse isotropy [35, 36]. Once the material properties of the fibre and matrix are known, the elastic material properties of the composite can be readily obtained by creating a simple homogenised representative volume element (RVE) [37]. The strength properties of the composite can be approximated by using the Rule of Mixture (ROM) in the longitudinal and transverse directions:

$$X_1 = V_f X_f + (1 - V_f) X_m \tag{3}$$

$$X_2 = \left(\frac{V_f}{X_f} + \frac{1 - V_f}{X_m} \right)^{-1} \tag{4}$$

In the above formulae, X represents the material properties of the composite, e.g. tensile strength or compressive strength, and the subscript 1 represents the longitudinal direction while 2 represents the transverse direction. Subscripts f and m refer to the fibre and matrix respectively; V_f is the fibre volume

fraction (FVF). It should be noted that the resulting composite strength estimates assume that the fibre and matrix are perfectly bonded. More information on determining the material properties can be found in [38].

4. Damage initiation and evolution

4.1 Constitutive model

The strain-based continuum damage model proposed by Linde [32] is capable of capturing the damage initiation of fibre reinforced composite as well as fibre-metal laminates [33, 39, 40]. However, it does not consider the contribution of the shear strain in the fibre direction to the damage initiation criterion. For the composite considered in this paper, the shearing effect in the fibre direction cannot be ignored since the continuous long fibre receives significant shear stress in the fibre direction under three-point bending, which is one of the dominant load cases when the implant is in-service in the body. Therefore, a modified model was adopted to assess the damage initiation and evolution of the composite in three-point bending [34], which is presented in this section. For the fibre, the damage initiates when the following criterion is met:

$$F_f = \sqrt{\frac{(\varepsilon_{11})^2}{\varepsilon_{11}^{f,t}\varepsilon_{11}^{f,c}} + \frac{\varepsilon_{11}^{f,c} - \varepsilon_{11}^{f,t}}{\varepsilon_{11}^{f,t}\varepsilon_{11}^{f,c}}\varepsilon_{11} + \left(\frac{\varepsilon_{12}}{\varepsilon_{12}^{f}}\right)^2} > 1 \tag{5}$$

where $\varepsilon_{11}^{f,t} = \sigma_L^{f,t}/C_{11}$, $\varepsilon_{11}^{f,c} = \sigma_L^{f,c}/C_{11}$ are the tensile and compressive failure strains in the fibre direction, respectively; $\sigma_L^{f,t}$ and $\sigma_L^{f,c}$ are the tensile and compressive strengths of the composite in the fibre direction, respectively; $C_{11}$is the stiffness modulus of the composite in the fibre direction; ε_{11} is the strain of the specimen in the fibre direction; $\varepsilon_{12}^{f} = \varepsilon_{12}^{f}/C_{44}$ is the failure strain for shear; σ_{12}^{f} is the shear strength and C_{44} is the shear modulus of the composite.

For the matrix, the damage initiation is governed by the criterion below:

$$F_m = \sqrt{\frac{(\varepsilon_{22})^2}{\varepsilon_{22}^{f,t}\varepsilon_{22}^{f,c}} + \frac{\varepsilon_{22}^{f,c} - \varepsilon_{22}^{f,t}}{\varepsilon_{22}^{f,t}\varepsilon_{22}^{f,c}}\varepsilon_{22} + \left(\frac{\varepsilon_{12}}{\varepsilon_{12}^{f}}\right)^2} > 1 \tag{6}$$

where $\varepsilon_{22}^{f,t} = \sigma_T^{f,t}/C_{22}$, $\varepsilon_{22}^{f,c} = \sigma_T^{f,c}/C_{22}$ are the tensile and compressive failure strains of the composite in the transverse direction, respectively; $\sigma_T^{f,t}$ and $\sigma_T^{f,c}$ are the tensile and compressive strengths of the composite in the transverse direction, respectively; $C_{22}$is the stiffness of the composite in the transverse direction.

The damage onset in the fibre and matrix are evaluated individually. Once the damage initiates, the degradation of the material properties is assumed to be under control of individual fracture energies, respectively:

$$d_f = 1 - \frac{\varepsilon_{11}^{f,t}}{F_f} e^{\left(-C_{11}\varepsilon_{11}^{f,t}\left(F_f - \varepsilon_{11}^{f,t}\right)L_c/G_f\right)} \tag{7}$$

$$d_m = 1 - \frac{\varepsilon_{22}^{f,t}}{F_m} e^{\left(-C_{22}\varepsilon_{22}^{f,t}\left(F_m - \varepsilon_{22}^{f,t}\right)L_c / G_m\right)} \tag{8}$$

where d_f and d_m are damage variables for the fibre and matrix, respectively; L_c represents the characteristic length of the element used in the modelling which is based on the element geometry and to alleviate mesh dependency during material softening [41], in the current model, the characteristic length at a material point is assumed equal to the square root of the area associated with it; G_f and G_m represent the fracture energy of the fibre and matrix, respectively, which can be determined experimentally from flexural tests [42]. The effective stiffness matrix of the composite is defined as follows:

$$C_d = C - \begin{bmatrix} d_f C_{11} & \left(d_f + d_m\right)C_{12}/2 & d_f C_{13}/2 & 0 & 0 & 0 \\ & d_m C_{22} & d_m C_{23}/2 & 0 & 0 & 0 \\ & & 0 & 0 & 0 & 0 \\ & sym. & & \left(d_f + d_m\right)C_{44}/2 & 0 & 0 \\ & & & & d_f C_{55}/2 & 0 \\ & & & & & d_m C_{66}/2 \end{bmatrix} \tag{9}$$

The effective stiffness matrix containing the damage parameters is symmetric, therefore a symmetric matrix storage can be adopted to reduce computational cost.

4.2 Numerical implementation

The criterion is implemented into a UMAT (user-defined material) subroutine in the commercial FE software ABAQUS to facilitate predicting composite failure under three-point bending. The UMAT subroutine includes three steps:

1. Newton-Raphson method is adopted in the main programme to obtain the local strain and pass the strain information to the UMAT. The UMAT determines whether damage is initiated and updates the stress and Jacobian matrix accordingly;
2. If damage is initiated, the damage variables are updated through a regularization technique and the stiffness is reduced accordingly. Updated stresses and strains, and the effective Jacobian matrix are evaluated;
3. The convergence status is checked in each increment. If convergence is achieved, the analysis advances to the next increment. Otherwise, the current increment size is reduced and the steps repeat until convergence.

At the beginning of each increment, stress, strain and other internal state variables (i.e. damage parameters) from the previous time increment are passed into the UMAT, including the strain increment. If damage is undetected then the damage parameter equals 0; if damage is detected in either the fibre or matrix, the effective stiffness matrix is adopted to update the stress and the Jacobian matrix. The stress-strain relationship after the onset of the damage can be expressed as:

$$\boldsymbol{\sigma} = \mathbf{C}_d : \boldsymbol{\varepsilon} \tag{10}$$

The Jacobian matrix can be obtained by differentiating Equation (10), since damage onset is a function of the fibre and matrix damage variables,

$$\begin{aligned}\frac{\partial \boldsymbol{\sigma}}{\partial \boldsymbol{\varepsilon}} &= \mathbf{C}_d + \frac{\partial \mathbf{C}_d}{\partial \boldsymbol{\varepsilon}} : \boldsymbol{\varepsilon} \\ &= \mathbf{C}_d + \left(\frac{\partial \mathbf{C}_d}{\partial d_m} : \boldsymbol{\varepsilon}\right)\left(\frac{\partial d_m}{\partial F_m}\frac{\partial F_m}{\partial \boldsymbol{\varepsilon}}\right) + \left(\frac{\partial \mathbf{C}_d}{\partial d_f} : \boldsymbol{\varepsilon}\right)\left(\frac{\partial d_f}{\partial F_f}\frac{\partial F_f}{\partial \boldsymbol{\varepsilon}}\right)\end{aligned} \tag{11}$$

In order to speed up convergence, a technique based on the viscous Duvaut-Lions regularization is implemented in the UMAT subroutine [43]. Considering the difference in the material properties of the fibre and matrix, two individual viscosity parameters are introduced. The damage variables are 'regularized' by using the following equations:

$$\frac{d\left(d_m^v\right)}{dt} = \frac{1}{\eta_m}\left(d_m - d_m^v\right) \tag{12}$$

$$\frac{d\left(d_f^v\right)}{dt} = \frac{1}{\eta_f}\left(d_f - d_f^v\right) \tag{13}$$

where d_m^v and d_f^v represent the 'regularized' damage variables used in real calculations to update the Jacobian matrix; η_m and η_f are the viscosity parameters for the matrix and fibre, respectively, controlling the rate at which the regularized damage variable approaches the true damage variables. In order to get the regularized damage variables at the time $t_0 + \Delta t$, the backward Euler method is used in the UMAT to discretize the above equations as:

$$d_m^v\Big|_{t_0+\Delta t} = \frac{\Delta t}{\eta_m + \Delta t} d_m\Big|_{t_0+\Delta t} + \frac{\eta_m}{\eta_m + \Delta t} d_m^v\Big|_{t_0} \tag{14}$$

$$d_f^v\Big|_{t_0+\Delta t} = \frac{\Delta t}{\eta_f + \Delta t} d_f\Big|_{t_0+\Delta t} + \frac{\eta_f}{\eta_f + \Delta t} d_f^v\Big|_{t_0} \tag{15}$$

The ratio of d_m^v over d_m and d_f^v over d_f can be easily obtained from above equations as:

$$\frac{\partial d_m^v}{\partial d_m} = \frac{\Delta t}{\eta_m + \Delta t} \tag{16}$$

$$\frac{\partial d_f^v}{\partial d_f} = \frac{\Delta t}{\eta_f + \Delta t} \tag{17}$$

Here the time increment Δt is determined by the auto-adaptive algorithm implemented in the UMAT, which is based on the algorithm in [44]. A trial value of the stress increment $\Delta\sigma_1$ is firstly calculated by

$$\Delta\boldsymbol{\sigma}_1 = \Delta t_n (\mathbf{C}_{d,n-1} + \frac{\partial \mathbf{C}_{d,n-1}}{\partial \boldsymbol{\varepsilon}_{n-1}} : \boldsymbol{\varepsilon}_{n-1}) : \Delta\boldsymbol{\varepsilon}_n \tag{18}$$

where n and $n-1$ represent the current step and the prior step, respectively. A second trial value of the stress increment $\Delta\sigma_2$ is calculated and the average of the two trial values is used to calculate the trial updated stress

$$\Delta\boldsymbol{\sigma}_2 = \Delta t_n (\mathbf{C}_{d,n-1} + \frac{\partial \mathbf{C}_{d,n}}{\partial \boldsymbol{\varepsilon}_n} : \boldsymbol{\varepsilon}_n) : \Delta\boldsymbol{\varepsilon}_n \tag{19}$$

$$\Delta\boldsymbol{\sigma} = \frac{1}{2}\left(\Delta\boldsymbol{\sigma}_1 + \Delta\boldsymbol{\sigma}_2\right) \tag{20}$$

$$\boldsymbol{\sigma}_n = \boldsymbol{\sigma}_{n-1} + \Delta\boldsymbol{\sigma} \tag{21}$$

The trial updated stress is evaluated by measuring the error indicator R_{error} as

$$R_{error} = \left\|\Delta\boldsymbol{\sigma}_2 - \Delta\boldsymbol{\sigma}_1\right\| / 2\left\|\Delta\boldsymbol{\sigma}\right\| \tag{22}$$

If R_{error} is smaller than the pre-set tolerance error *RTOL*, the updated stress is accepted, which means the increment size is valid. If the R_{error} is greater than the threshold, then a smaller sub-increment is determined based on R_{error} and the sub-increment tolerance, *STOL*, as

$$\Delta t_{n+1} = \sqrt{\frac{STOL}{R_{error}}}\Delta t_n \tag{23}$$

where

$$\Delta t_n = \min\left\{\Delta t_n^1, 1-T\right\} \tag{24}$$

$$\Delta t_n^1 = \max\left\{q\Delta t_n^0, \Delta t_{\min}\right\} \tag{25}$$

$$q = \max\left\{0.9\left(\frac{STOL}{R_{error}}\right)^{1/2}, 0.1\right\} \tag{26}$$

In the above formulae, T is the pseudo increment size ranging from 0 to 1, Δt_{min} is the preset minimum increment size and Δt_n^0 is the original increment size adopted in the calculation of the trial stress increment. The auto-adaptive algorithm guarantees that the increment size is constrained by a pre-set accuracy requirement.

For a certain value of Δt, a large value for η results in a noticeable gap between the regularized damage variable and the true damage variable, which might cause a delay in the degradation of the Jacobian matrix as shown below:

$$\frac{\partial\boldsymbol{\sigma}}{\partial\boldsymbol{\varepsilon}} = \mathbf{C}_d + \left[\left(\frac{\partial \mathbf{C}_d}{\partial d_m} : \boldsymbol{\varepsilon}\right)\left(\frac{\partial d_m}{\partial F_m}\frac{\partial F_m}{\partial \boldsymbol{\varepsilon}}\right)\right]\frac{\Delta t}{\eta_m + \Delta t} + \left[\left(\frac{\partial \mathbf{C}_d}{\partial d_f} : \boldsymbol{\varepsilon}\right)\left(\frac{\partial d_f}{\partial F_f}\frac{\partial F_f}{\partial \boldsymbol{\varepsilon}}\right)\right]\frac{\Delta t}{\eta_f + \Delta t} \tag{27}$$

Equation (27) is the final form adopted in the UMAT to update the Jacobian matrix at the end of one increment when either form of damage is initiated. The viscous regularized Jacobian matrix can improve

the convergence, however, unrealistic results due to viscous regularization should be avoided. To assess the viscous regularization, the approximate amount of energy associated with viscous regularization is integrated incrementally in the UMAT by updating the variables SCD as follows:

$$\Delta E_{SCD} = \frac{1}{2}\left[\left(\mathbf{C}_d : \boldsymbol{\varepsilon}\right)\Big|_{t_0} + \left(\mathbf{C}_d : \boldsymbol{\varepsilon}\right)\Big|_{t_0+\Delta t}\right] : d\boldsymbol{\varepsilon} - \frac{1}{2}\left[\left(\mathbf{C}_d^0 : \boldsymbol{\varepsilon}\right)\Big|_{t_0} + \left(\mathbf{C}_d^0 : \boldsymbol{\varepsilon}\right)\Big|_{t_0+\Delta t}\right] : d\boldsymbol{\varepsilon} \tag{28}$$

where $\boldsymbol{C}_d$ and $\boldsymbol{C}_d^0$ represent the effective stiffness matrix calculated using the regularized damage variables and the true damage variable values respectively; ΔE_{SCD} is the difference between the energies calculated by $\boldsymbol{C}_d$ and $\boldsymbol{C}_d^0$. ΔE_{SCD} should be small compared to the other real energies available in the main programme, e.g. the strain energy ALLSE. The whole flow of the numerical implementation, including the automatic control of the incremental step size, is illustrated in Figure 1. More information about this can be found in [44].

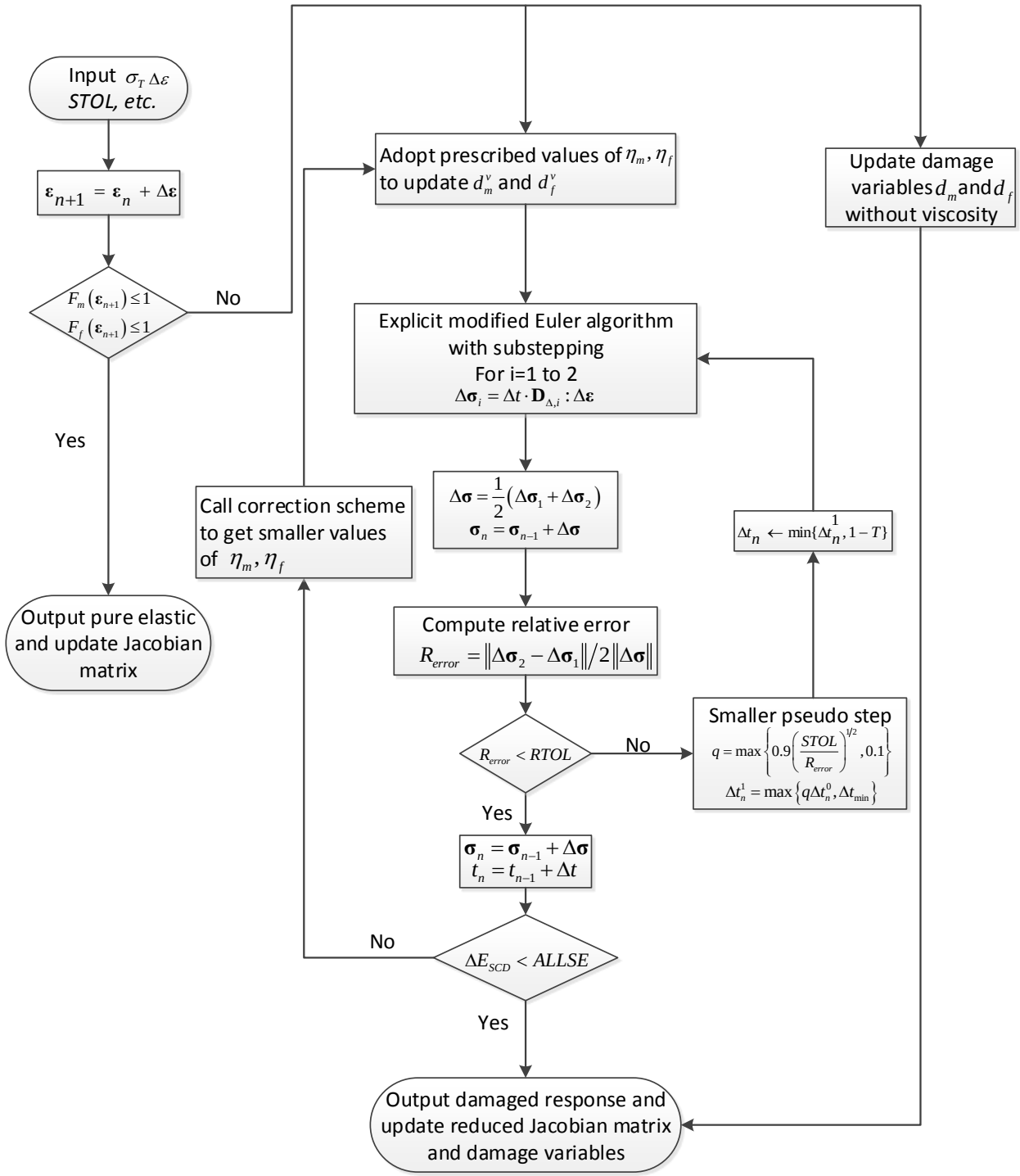

Figure 1 The whole flow of the auto-adaptive algorithm.

5. Numerical modelling

5.1 Material properties and boundary conditions

The constitutive model was adopted to simulate the experimental data of composite with FVF of 20%, 35% and 50%. The tested composites were manufactured by the in-situ polymerization (ISP) method [9].

The mechanical properties of the composite are primarily determined by the properties of the fibre and matrix, but are also influenced by the manufacturing method, i.e. the quality of the bonding interface. In this paper, the material parameters required in the constitutive model were determined by using the aforementioned homogenization method and ROM. The material properties utilized in the numerical modelling are listed in Table 1. Despite the absence of some specifications of the fibre and matrix, the mechanical properties of the fibre and matrix can be evaluated from the static properties of the composite through numerical modelling. The fracture energies of the fibre and matrix were estimated to be 12.5 N/m and 1 N/m, respectively [33]. The viscosity parameters for the fibre and matrix were selected as 0.001 and 0.005, respectively [39]. The load was applied at the centre of the specimen vertically downwards, while the specimen was placed on two supports with a span of 32mm. The contact between the supports and the bottom surface was modelled as a "hard contact" and sliding at the contact point was allowed. Throughout the numerical test, displacements in the other two principal directions were constrained. The layout of the model is illustrated in Figure 2.

Table 1 Material properties input in the numerical modelling. Direction 1 in the table means the fibre direction, and direction 2 and 3 are the two directions perpendicular to the fibre direction.

Fibre volume fraction	**20%**	**35%**	**50%**
Young's modulus in direction 1, E_1	8356 MPa	14299 MPa	21295 MPa
Young's modulus in direction 2, E_2	229 MPa	291 MPa	378 MPa
Shear modulus in 1-2 plane, G_{12}	198 MPa	253 MPa	286 MPa
Shear modulus in 2-3 plane, G_{23}	108 MPa	138 MPa	211 MPa
Poisson ratio in 1-2 direction, ν_{12}	0.25	0.25	0.25
Poisson ratio in 2-3 direction, ν_{23}	0.25	0.25	0.25
Tensile strength in direction 1, S_t^1	70 MPa	110 MPa	140 MPa
Compressive strength in direction 1, S_c^1	46.5 MPa	88 MPa	124.1 MPa
Tensile strength in direction 2, S_t^2	15.8 MPa	19.1 MPa	24.2 MPa
Compressive strength in direction 2, S_c^2	50 MPa	50 MPa	50 MPa
Shear strength in 1-2 plane, S_s^{12}	15.8 MPa	15.8 MPa	15.8 MPa
Fracture energy of the matrix, G_m [33]	1 N/m	1 N/m	1 N/m
Fracture energy of the fibre, G_f [33]	12.5 N/m	12.5 N/m	12.5 N/m
Viscosity parameter, η_f [39]	0.001	0.001	0.001
Viscosity parameter, η_m [39]	0.005	0.005	0.005
Sub-increment tolerance, *STOL*	0.0001	0.0001	0.0001
Relative error tolerance, *RTOL*	0.001	0.001	0.001
Pseudo increment size, *T*	0.9	0.9	0.9
Minimum increment step size, Δt_{min}	0.01	0.01	0.01

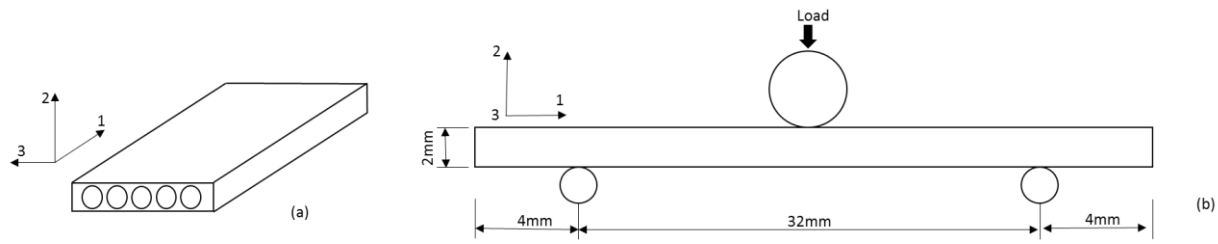

Figure 2 (a) Illustration of the coordinate system; (b) layout of the three-point bending.

5.2 Mesh sensitivity analysis

A suitable mesh size needs to be determined to achieve a balance between computational efficiency and model accuracy. Figure 3 shows the variations in stress-strain curve obtained using different mesh densities. It shows that the initial stiffness is negligibly affected by the mesh density, however there are clear differences between the three mesh densities once failure has initiated. The coarse mesh (4800 elements) does not predict as close result as other two meshes, while the finest mesh (12000 elements) generates quite a close result with the intermediate mesh but requires more computation cost. Upon a balance between the computation efficiency and accuracy, 9600 elements (global size 0.25) was selected for the numerical simulations in the following sections.

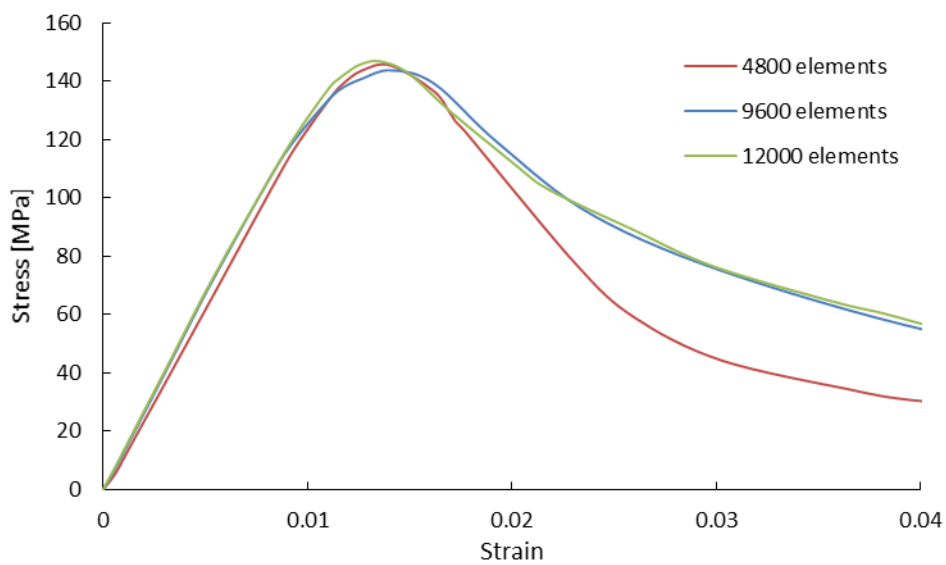

Figure 3 The variation of the stress-strain relationship of the numerical results with different element numbers, 35% FVF.

5.3 Numerical results and discussion

5.3.1 Sensitivity analysis of tensile and compressive strength

In three-point bending, the top surface of the specimen is under compression while the bottom surface is under tension. From experimental studies, the top surface of the specimen suffered the most damage [45], and thus the compressive strength in the fibre direction is assumed to be significant. On the other hand, the tensile strength in the fibre direction is more important in the bottom surface area. In order to investigate the pattern that the tensile and compressive strength in the fibre direction affect the flexural strength, two groups of numerical experiments were carried out. In these numerical experiments, the tensile and compressive strength in the fibre direction of the composite were varied, while the other material parameters remained the same. The intermediate FVF (35%) was selected as the reference case. The controlled material properties are listed in Table 2 and Table 3.

Table 2 Material properties utilized in the numerical simulations on the influence of the compressive strength in fibre direction.

	Set-1 (MPa)	**Set-2 (MPa)**	**Set-3 (MPa)**
Tensile strength in direction 1, S_t^1	110	110	110
Compressive strength in direction 1, S_c^1	88	75	60

Table 3 Material properties utilized in the numerical simulations on the influence of the tensile strength in fibre direction.

	Set-1 (MPa)	**Set-2 (MPa)**	**Set-3 (MPa)**
Tensile strength in direction 1, S_t^1	110	95	80
Compressive strength in direction 1, S_c^1	88	88	88

Figure 4(a) shows the stress-strain relation of the composite with different compressive strengths in the fibre direction. The failure strain (the strain at which the peak stress occurs) of the composite decreased by 12.6% when the compressive strength in fibre direction decreased by 14.8% from Set-1 to Set-2.There was a further reduction in composite failure strain of 11.0% when the compressive strength in fibre direction decreases by 23.1% between Set-2 and Set-3. The flexural strength also decreased with smaller compressive strength in the fibre direction. The flexural strength of Set-2 was 6.8% smaller than Set-1, and Set-3 was 7.7% smaller than Set-2. The numerical simulations showed that the compressive strength in the fibre direction has a significant influence on both the flexural strength and failure strain of the composite.

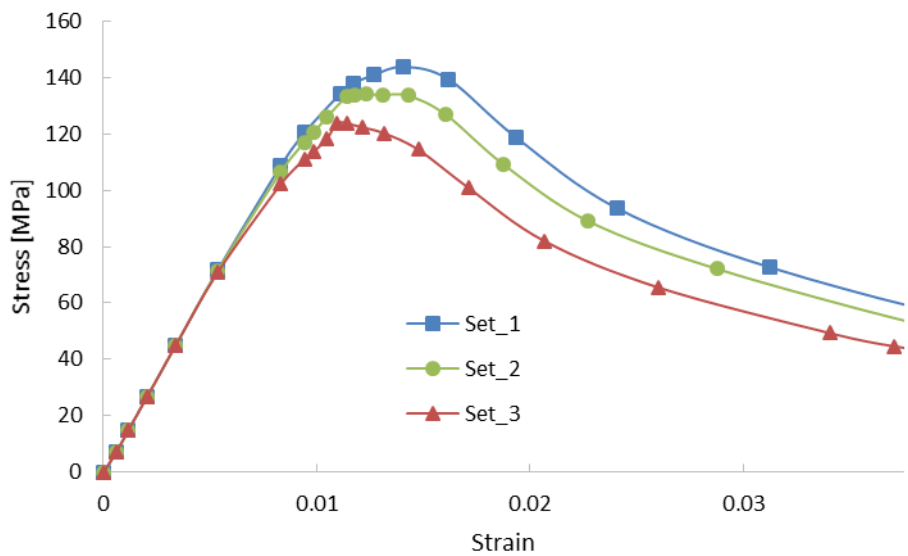

(a)

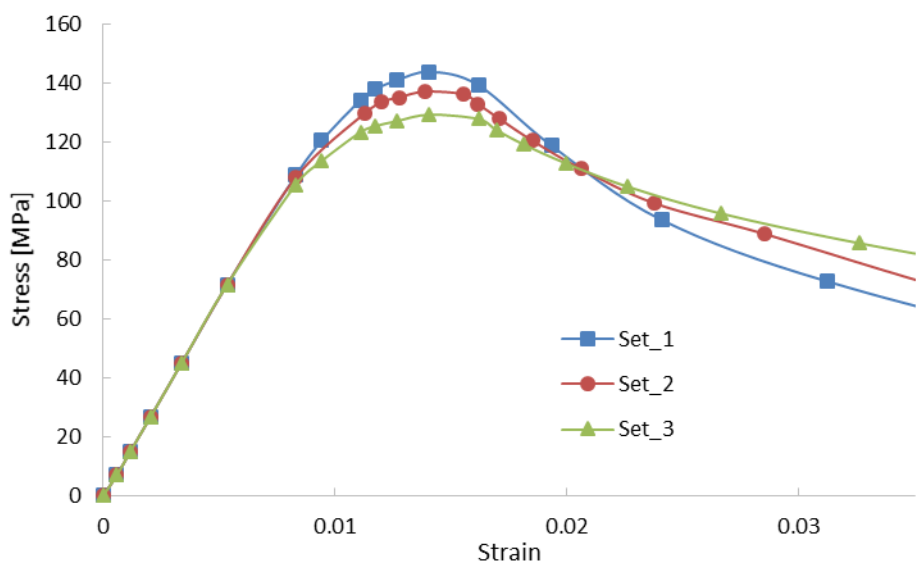

(b)

Figure 4 Sensitivity study of the numerically predicted flexural strength of the composites, 35% FVF: (a) the influence of the compressive strength; (b) the influence of the tensile strength.

The sensitivity study of the tensile strength of the composite in fibre direction is presented in Figure 4(b). It showed that the flexural strength of the composite increased with higher tensile strength in the fibre direction. The flexural strength of the composite increased by 6.01% when the tensile strength of the material increased by 18.75% from Set-3 to Set-2. An increment of 4.88% in the flexural strength was observed when the tensile strength increased by 15.79% from Set-1 to Set-2. The positive trend between the flexural strength and the tensile strength was the same as the compressive strength, however, the tensile strength had negligible influence on the failure strain. There was only 1.36% and 1.38% difference in the failure strain between Set-2 and Set-3, and between Set-2 and Set-1, respectively. The two groups

of numerical simulations showed the influence of the tensile and compressive strength in the fibre direction. The compressive strength in the fibre direction affected the performance of the composite more significantly than the tensile strength. The later sections reveal that the top surface of the composite was the most vulnerable under three-point bending, and the damage was initiated from the top surface. The composite properties can be managed according to actual needs, for instance, increasing either the compressive or tensile strength of the composite can improve the flexural strength, whereas increasing the compressive strength can improve the failure strain at the same time. Understanding of how the components influence the overall performance of the composite can, in return, offer guidance to the manufacturing of the composite.

5.3.2 Damage variables of the fibre d_f and matrix d_m

Investigation of the damage onset and evolution in the fibre and matrix is presented in this section. Figure 5 shows the damage variables for the fibre and matrix of the composites with different FVF. The damage initiation and evolution in the middle of the top surface was presented, which was the compressed area. The damage in the fibre initiated ahead of the matrix, however, the gap decreased with increasing FVF. For composite with 20% FVF, the damage in the matrix initiated at the strain about 0.025, whilst it was about 0.020 when the FVF was 35%, and it was about 0.018 when FVF was 50%. Unlike in the matrix, damage in the fibre initiated at nearly the same strain for all three composite about 0.060. Fibre damage evolved more significantly with increasing strain for composites with higher FVF. As shown that when the failure of the sample occurred the damage index of the matrix had not accumulated to 1 while the index of the fibre had reached 1, which indicated that the fibre damage accumulation was the primary driver of the composite flexural failure.

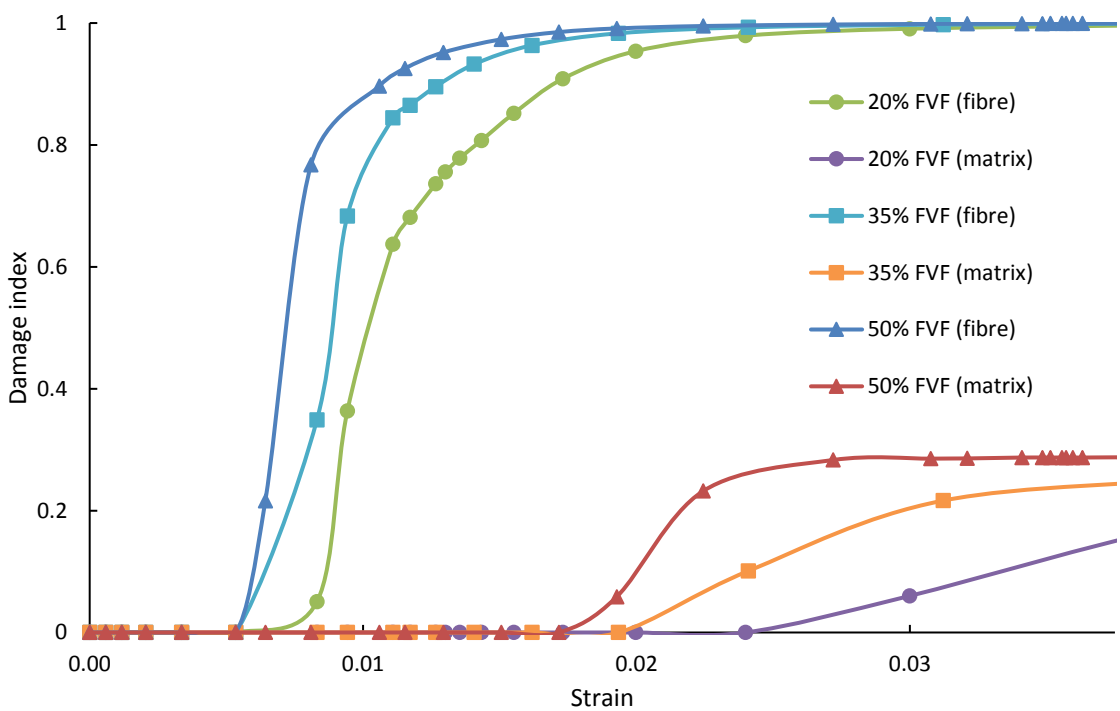

Figure 5 The damage initiation and evolution in the fibre and matrix for composites with different FVF.

5.3.3 Numerical model validation

Figure 6 compares the stress-strain curve obtained from the FE analysis with the experimental data, for composite with 35% FVF. A good agreement between the experimental data and numerical results was achieved, with the relative errors for the flexural modulus, flexural strength and failure strain being less than 3% (see Table 4). In the first stage of the experiment, the specimen was in the elastic regime, so the experimental stress-strain relationship was linear. The numerical results also demonstrated the linear stress-strain relation in the first stage and the stiffness was in good agreement (3.0% relative error) with the experimental data. The softening initiation at the end of the elastic regime of the specimen was caused by the damage onset in the specimen, as marked in Figure 6. The second stage of the stress-strain relationship was from the damage onset to the flexural strength. In this stage, the specimen had not yet failed, but damage accumulation softened the response of the specimen. The remaining curve representing the third stage, which described the mechanical behaviour of the specimen post failure. In Figure 6, the numerical flexural strength (143.81 MPa) agreed well with the experimental data (146.31 MPa). The agreement of the flexural strength between the numerical results and the experimental data showed the accuracy (relative error 1.71%) of the constitutive model in simulating the flexural strength of the specimen in three-point bending. Moreover, the failure strain in numerical results was 0.0125, which was in excellent agreement (relative error 0.81%) with the experimental data, 0.0124.

Table 4 Comparison of the numerical results with experimental data, 35% FVF.

	Experimental	Numerical	Relative errors (%)
Flexural strength	146.31 MPa	143.81 MPa	1.71
Failure strain	0.0124	0.0125	0.81
Flexural modulus	13.65 GPa	14.06 GPa	3.00

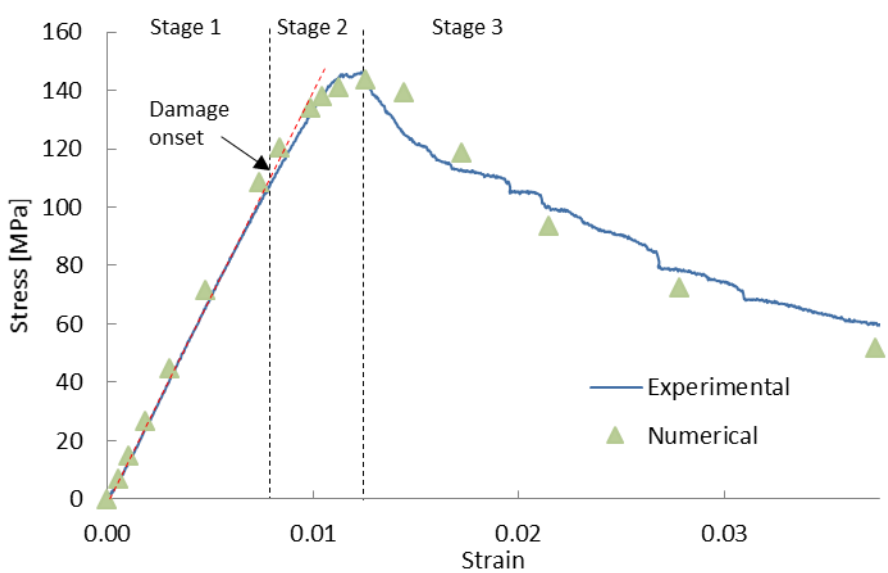

Figure 6 Comparison between the numerical results and experimental results of the composite, 35% FVF.

The adopted constitutive model was capable of capturing the damage initiation and evolution of the fibre and matrix individually, which was important for the purpose of understanding the mechanism of composites failure under three-point bending. Figure 7 (a), (b) show the damage status of the fibre and matrix at the point when damage onset was detected. It can be observed that damage occurred in the fibre first, whilst the matrix remained undamaged. The observation is consistent with the fact that although the matrix is not as stiff as the fibre, it has a higher failure strain before irreversible damage occurs. Figure 7 (c), (d) show the damage initiation in the matrix and the damage accumulation in the fibre at the same time. It can be seen that when damage was initiated in the top surface area of the matrix, the damaged area in the fibre had evolved from the top to the bottom, and the total damaged area had also grown significantly. From Figure 7, it can be concluded that for the fibre and matrix investigated in this paper, damage in both the fibre and matrix were initiated from the top area of the specimen and then propagated to the bottom of the sample. The failed sample shown in Figure 8 show the damage accumulation in the top surface during the three-point bending, due to the fibre buckling in compression, was more dramatic than the damage accumulation in the bottom, due to fibre fracture in tension.

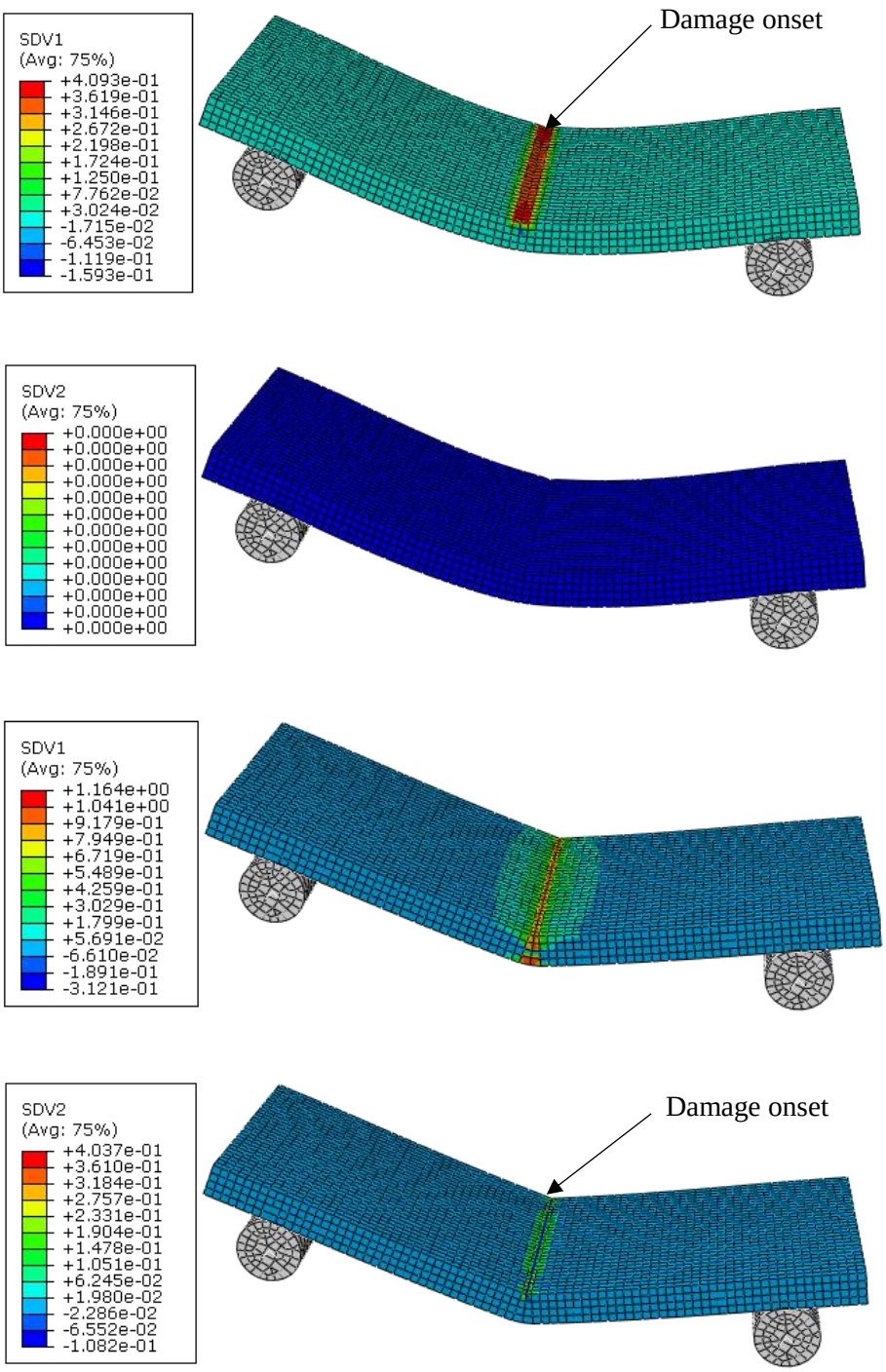

(a)

(b)

(c)

(d)

Figure 7 The damage status of the specimen at the onset of matrix damage, applied vertical displacement 1.2mm, 35% FVF: (a) Damage index contour for the fibre when damage onset is detected in the fibre; (b) Damage status for the matrix when damage onset is detected in the fibre; (c) Damage index contour for the fibre when damage onset is detected in the matrix; (d) Damage index contour for the matrix when damage onset is detected in the matrix.

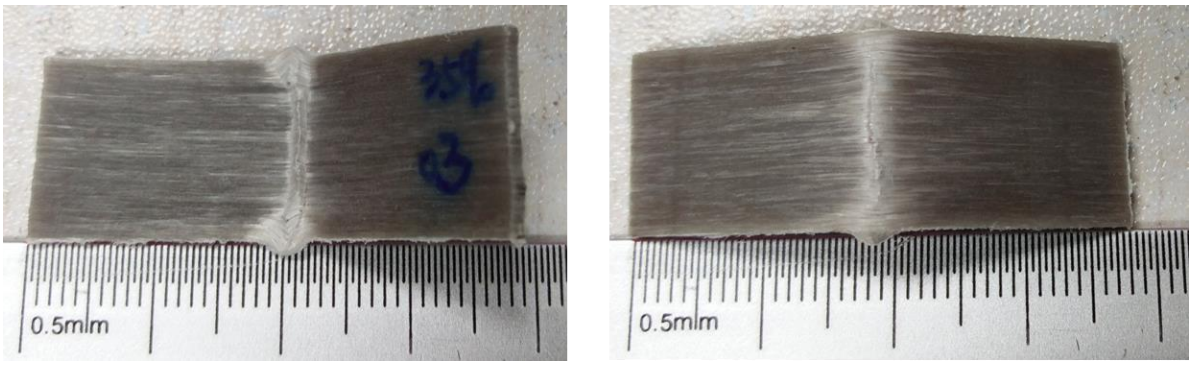

(a) (b)

Figure 8 Failed sample after three-point bending, 35% FVF: (a) the top surface; (b) the bottom surface.

Figure 9 (a) shows a comparison of the numerical results and the experimental data for a specimen with a FVF of 20%. It can be seen that the numerical results agreed well with the experimental data in the elastic region (relative error 1.79%) and the flexural strength was within 1.0% of the experimental data. However, there was relatively poor agreement in the failure strain (relative error 5.84%) and a mismatch in the post-damage region (see Table 5). Damage propagation appeared to be more sudden according to the experimental curve, with a dramatic reduction in stress at a strain of 0.014. The numerical data indicated a more progressive reduction in strength beyond the ultimate strength. The SEM in Figure 9 (b) shows that there were many detached fibres after failure occurred. The detached fibres lost the reinforcing ability and, hence, reduced the stiffness of the composite dramatically post failure. The reduction in stiffness was therefore due to debonding rather than fibre fracture. However, for the numerical result, the reduction in stiffness was associated with fibre damage accumulation rather than interfacial failure, which had been overlooked in the current model since a perfect fibre/matrix bond had been assumed.

Table 5 Comparison of the numerical results with experimental data, 20% FVF.

	Experimental	**Numerical**	**Relative errors (%)**
Flexural strength	88.65 MPa	87.76 MPa	1.00
Failure strain	0.0137	0.0145	5.84
Flexural modulus	6.69 GPa	6.81 GPa	1.79

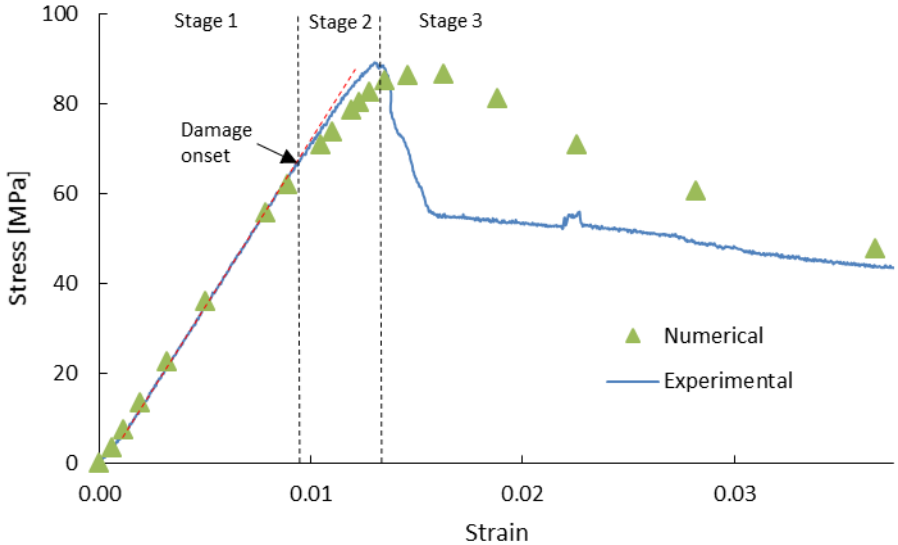

(a)

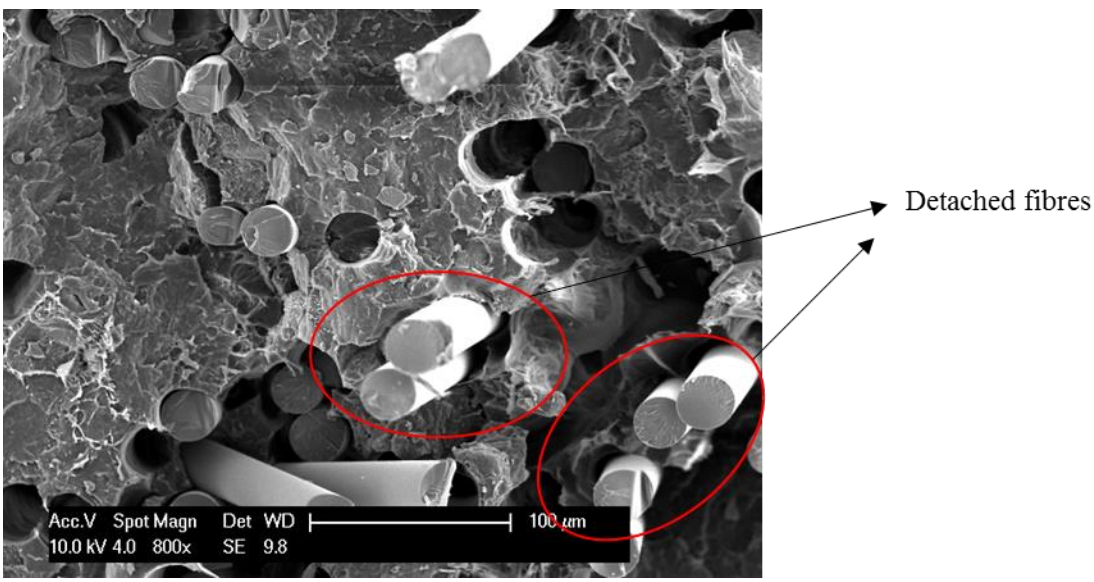

(b)

Figure 9 (a) Comparison between the numerical results and experimental results of the composite, 20% FVF; (b) The detached fibres in the failed composite, 20% FVF.

The comparison between the numerical result and experimental data of the composite with FVF of 50% is presented in Figure 10. The numerical result agreed well (relative error 4.44%) with the experimental data in Stage 1. A good fit (relative error 1.74%) was found in the flexural strength prediction as well (see Table 6). However, poor agreement was observed for the failure strain predictions, which were approximately 9% higher than the experimental value. This was because the model parameters (e.g. fracture energy G_f and G_m) were validated using the 35% fibre volume faction data. It should also be noted that for the experimental data, there was a plateau region following the initial stress reduction after the peak. This 'plastic-like' phenomenon can be attributed to dry fibre bundles, see Figure 10 (b), which

were more common to find in composites with high FVF. Once the specimen had failed, these dry bundles could slide more easily at higher applied strains.

Table 6 Comparison of the numerical results with experimental data, 50% FVF.

	Experimental	Numerical	Relative errors (%)
Flexural strength	192.80 MPa	189.45 MPa	1.74
Failure strain	0.0124	0.0135	8.87
Flexural modulus	17.33 GPa	16.53 GPa	4.44

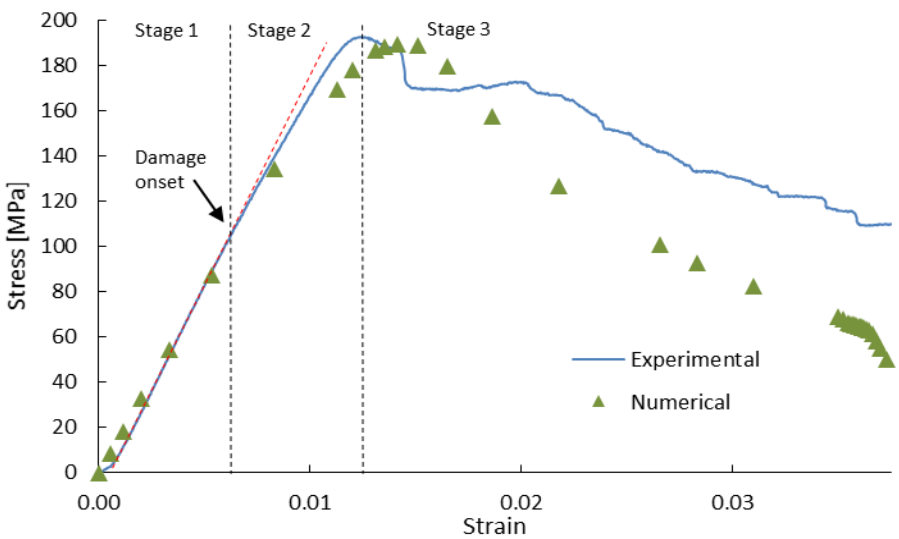

(a)

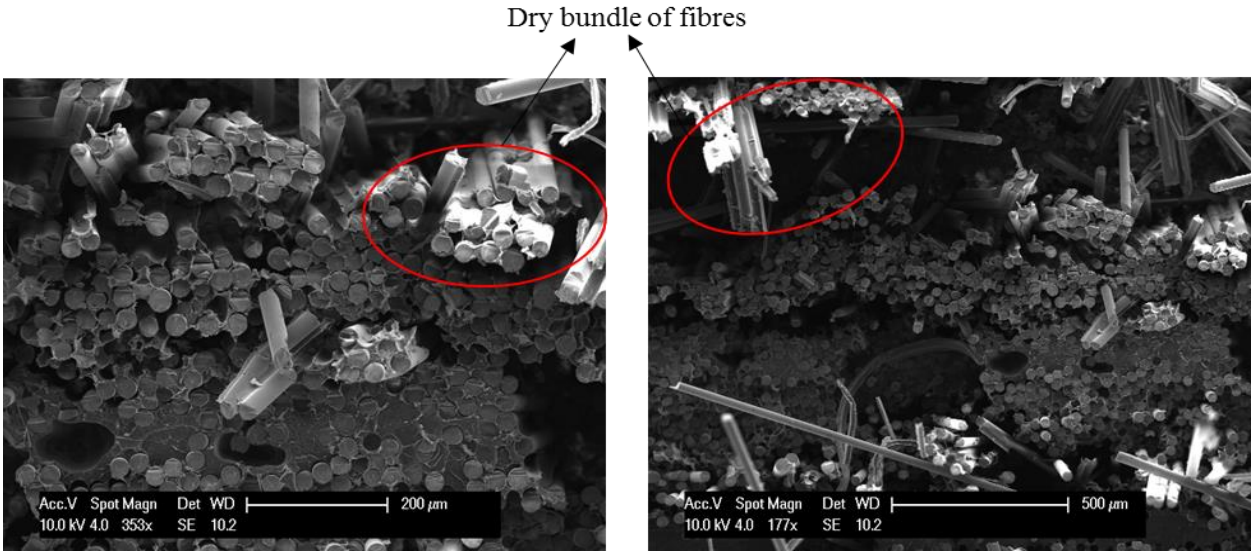

(b)

Figure 10 (a) Comparison between the numerical results and experimental results of the composite, 50% FVF; (b) Dry bundle of fibres in high volume fraction composite, 50% FVF.

6. Conclusions

In this paper, a constitutive model from the literature based on Linde's criterion was adopted to simulate the stress-strain relationship of a fully bio-resorbable composite under three-point bending. Two viscosity parameters were used to regularize the damage variables, hence to improve the convergence, along with an auto-adaptive algorithm to control the incremental step size. The FE model was capable of outputting the damaged stress-strain relationship of the composite and the damage onset and evolution in the fibre and matrix individually. Comparisons between the numerical results and experimental data indicated that

1. The FE model was capable of predicting the behaviour of the composite under three-point bending. The elastic stage of the stress-strain relation predicted by the FE model was in excellent agreement with the experimental data (less than 4.5% relative error in all cases).
2. The absolute flexural strength of the composite was predicted within 2% for all of the FVF studied (20%, 35% and 50%). The prediction of failure strain was relative poor, within 9% of the experimental values, since the model neglected fibre debonding.
3. The sensitivity analysis revealed that both the tensile and compressive strength in the fibre direction of the composite affects the flexural strength. The fibre compressive strength also affected the composite failure strain, but the fibre tensile strength did not.
4. The investigation on the individual damage onset and evolution in the fibre and matrix showed that both damages were initiated from the top then propagated to the bottom, however, the damage in the fibre was initiated prior to that in the matrix. It was noted that the main driver of the composite failure under three-point bending was the damage accumulation in the fibre.

However, the model presented in this paper has defects in predicting the post peak stress-strain relationship for FVF of 20% and 50% comparing with the prediction for FVF of 35%. A more thorough model should be built in the future based on the current one to consider the fibre debonding and the formation of dry fibre bundles, such that to overcome the defects.

Acknowledgement

The authors would like to acknowledge support received from the International Doctoral Innovation Center (IDIC) at the University of Nottingham Ningbo China.

References

1. Engh, C.A., J. Bobyn, and A.H. Glassman, *Porous-coated hip replacement. The factors governing bone ingrowth, stress shielding, and clinical results.* Bone & Joint Journal, 1987. **69**(1): p. 45-55.
2. Huiskes, R., H. Weinans, and B. Van Rietbergen, *The relationship between stress shielding and bone resorption around total hip stems and the effects of flexible materials.* Clinical orthopaedics and related research, 1992. **274**: p. 124-134.
3. Nagels, J., M. Stokdijk, and P.M. Rozing, *Stress shielding and bone resorption in shoulder arthroplasty.* Journal of shoulder and elbow surgery, 2003. **12**(1): p. 35-39.
4. Parsons, A.J., et al., *Phosphate Glass Fibre Composites for Bone Repair.* Journal of Bionic Engineering, 2009. **6**(4): p. 318-323.
5. Casteleyn, P., F. Handelberg, and P. Haentjens, *Biodegradable rods versus Kirschner wire fixation of wrist fractures. A randomised trial.* Journal of Bone & Joint Surgery, British Volume, 1992. **74-B**(6): p. 858-861.

6. van Manen, C.J., et al., *Bio-resorbable versus metal implants in wrist fractures: a randomised trial.* Archives of Orthopaedic and Trauma Surgery, 2008. **128**(12): p. 1413.
7. Törmälä, P., T. Pohjonen, and P. Rokkanen, *Bioabsorbable polymers: materials technology and surgical applications.* Proceedings of the Institution of Mechanical Engineers, Part H: Journal of Engineering in Medicine, 1998. **212**(2): p. 101-111.
8. Hoffmann, J., et al., *A totally bioresorbable fibrillar reinforced composite system: structure and properties.* International Journal of Polymeric Materials, 2001. **50**(3-4): p. 469-482.
9. Chen, M., et al., *In-situ polymerisation of fully bioresorbable polycaprolactone/phosphate glass fibre composites: In vitro degradation and mechanical properties.* Journal of the Mechanical Behavior of Biomedical Materials, 2016. **59**: p. 78-89.
10. Felfel, R.M., et al., *Cytocompatibility, degradation, mechanical property retention and ion release profiles for phosphate glass fibre reinforced composite rods.* Materials Science and Engineering: C, 2013. **33**(4): p. 1914-1924.
11. Bitar, M., et al., *Soluble phosphate glasses: in vitro studies using human cells of hard and soft tissue origin.* Biomaterials, 2004. **25**(12): p. 2283-2292.
12. Parsons, A., et al., *Synthesis and degradation of sodium iron phosphate glasses and their in vitro cell response.* Journal of Biomedical Materials Research Part A, 2004. **71**(2): p. 283-291.
13. Felfel, R., et al., *In vitro degradation, flexural, compressive and shear properties of fully bioresorbable composite rods.* Journal of the mechanical behavior of biomedical materials, 2011. **4**(7): p. 1462-1472.
14. Liu, X., et al., *Magnesium coated bioresorbable phosphate glass fibres: investigation of the interface between fibre and polyester matrices.* BioMed research international, 2013. **2013**.
15. Sharmin, N., et al., *Structure, viscosity and fibre drawing properties of phosphate-based glasses: effect of boron and iron oxide addition.* Journal of Materials Science, 2016. **51**(16): p. 7523-7535.
16. Mannocci, F., M. Sherriff, and T.F. Watson, *Three-Point Bending Test of Fiber Posts.* Journal of Endodontics, 2001. **27**(12): p. 758-761.
17. Steeves, C.A. and N.A. Fleck, *Collapse mechanisms of sandwich beams with composite faces and a foam core, loaded in three-point bending. Part II: experimental investigation and numerical modelling.* International Journal of Mechanical Sciences, 2004. **46**(4): p. 585-608.
18. Harper, L.T., et al., *Finite element modelling of the flexural performance of resorbable phosphate glass fibre reinforced PLA composite bone plates.* Journal of the Mechanical Behavior of Biomedical Materials, 2012. **15**(Supplement C): p. 13-23.
19. Mishnaevsky Jr, L. and P. Brøndsted, *Micromechanical modeling of damage and fracture of unidirectional fiber reinforced composites: A review.* Computational Materials Science, 2009. **44**(4): p. 1351-1359.
20. Tserpes, K., et al., *Strength prediction of bolted joints in graphite/epoxy composite laminates.* Composites Part B: Engineering, 2002. **33**(7): p. 521-529.
21. Lu, J., W. Sun, and A. Becker, *Material characterisation and finite element modelling of cyclic plasticity behaviour for 304 stainless steel using a crystal plasticity model.* International Journal of Mechanical Sciences, 2016. **105**: p. 315-329.
22. Lu, J., et al., *Simulation of the fatigue behaviour of a power plant steel with a damage variable.* International Journal of Mechanical Sciences, 2015. **100**: p. 145-157.
23. Hill, R. *A theory of the yielding and plastic flow of anisotropic metals*. in *Proceedings of the Royal Society of London A: Mathematical, Physical and Engineering Sciences*. 1948. The Royal Society.
24. Tsai, S.W., *Strength Characteristics of Composite Materials*. 1965, Philco Corp Newport Beach CA.
25. Hoffman, O., *The brittle strength of orthotropic materials.* Journal of Composite Materials, 1967. **1**(2): p. 200-206.

26. Matzenmiller, A., J. Lubliner, and R.L. Taylor, *A constitutive model for anisotropic damage in fiber-composites.* Mechanics of Materials, 1995. **20**(2): p. 125-152.
27. Hashin, Z., *Fatigue failure criteria for unidirectional fiber composites.* ASME, Transactions, Journal of Applied Mechanics, 1981. **48**: p. 846-852.
28. Xu, K. and X.W. Xu, *Finite element analysis of mechanical properties of 3D five-directional braided composites.* Materials Science and Engineering: A, 2008. **487**(1): p. 499-509.
29. Zhou, Y., Z. Lu, and Z. Yang, *Progressive damage analysis and strength prediction of 2D plain weave composites.* Composites Part B: Engineering, 2013. **47**: p. 220-229.
30. Fang, G., et al., *Investigation on the compressive properties of the three dimensional four-directional braided composites.* Composite Structures, 2011. **93**(2): p. 392-405.
31. Murakami, S., *Notion of continuum damage mechanics and its application to anisotropic creep damage theory.* ASME, Transactions, Journal of Engineering Materials and Technology, 1983. **105**: p. 99-105.
32. Linde, P., et al. *Modelling and simulation of fibre metal laminates*. in *ABAQUS Users' conference*. 2004.
33. Lu, Z., B. Xia, and Z. Yang, *Investigation on the tensile properties of three-dimensional full five-directional braided composites.* Computational Materials Science, 2013. **77**: p. 445-455.
34. Wang, C., et al., *Development of a new constitutive model considering the shearing effect for anisotropic progressive damage in fiber-reinforced composites.* Composites Part B: Engineering, 2015. **75**: p. 288-297.
35. Castellano, A., et al., *Mechanical characterization of CFRP composites by ultrasonic immersion tests: Experimental and numerical approaches.* Composites Part B: Engineering, 2014. **66**(Supplement C): p. 299-310.
36. Mortazavian, S. and A. Fatemi, *Effects of fiber orientation and anisotropy on tensile strength and elastic modulus of short fiber reinforced polymer composites.* Composites Part B: Engineering, 2015. **72**(Supplement C): p. 116-129.
37. Barbero, E.J., *Finite element analysis of composite materials using AbaqusTM*. 2013: CRC press.
38. Gao, X., et al. *Numerical interpretation of fully bio-resorbable glass fibre reinforced composites*. in *International Conference on Composite Materials 21 (ICCM-21)*. 2017. Xi'an, China.
39. Lapczyk, I. and J.A. Hurtado, *Progressive damage modeling in fiber-reinforced materials.* Composites Part A: Applied Science and Manufacturing, 2007. **38**(11): p. 2333-2341.
40. Sadighi, M., et al., *Experimental and numerical investigation of metal type and thickness effects on the impact resistance of fiber metal laminates.* Applied Composite Materials, 2012. **19**(3-4): p. 545-559.
41. Manual, A.U., *Version 6.10.* ABAQUS Inc, 2010.
42. Guinea, G.V., J. Planas, and M. Elices, *Measurement of the fracture energy using three-point bend tests: Part 1—Influence of experimental procedures.* Materials and Structures, 1992. **25**(4): p. 212-218.
43. Lions, J.L. and G. Duvaut, *Inequalities in mechanics and physics*. 1976: Springer.
44. Abbo, A., *Finite element algorithms for elastoplasticy and consolidation*. 1997, University of Newcastle Upon Tyne.
45. Shibata, S., Y. Cao, and I. Fukumoto, *Flexural modulus of the unidirectional and random composites made from biodegradable resin and bamboo and kenaf fibres.* Composites Part A: Applied Science and Manufacturing, 2008. **39**(4): p. 640-646.